Research Square

Preprints are preliminary reports that have not undergone peer review.
They should not be considered conclusive, used to inform clinical practice,
or referenced by the media as validated information.

Parametric Study and Deposition Mechanism of Sn–Zn Coatings Fabricated by Underwater Cold Spray

Yuxian Meng

meng.yuxian@rs.tus.ac.jp

Tokyo University of Science: Tokyo Rika Daigaku https://orcid.org/0009-0006-3206-0616

Hiroki Saito

Chrystelle A. Bernard

Yuji Ichikawa

Kazuhiro Ogawa

Research Article

Keywords: underwater cold spray, Sn–Zn coating, water film, gas–water interaction, deposition efficiency, impact simulation

Posted Date: November 10th, 2026

DOI: https://doi.org/10.21203/rs.3.rs-11439688/v1

License: This work is licensed under a Creative Commons Attribution 4.0 International License.
Read Full License

Parametric Study and Deposition Mechanism of Sn–Zn Coatings Fabricated by Underwater Cold Spray

Yuxian Meng[1, *], Hiroki Saito[1], Chrystelle A. Bernard[1,2], Yuji Ichikawa[1], Kazuhiro Ogawa[1]

[1]Fracture and Reliability Research Institute, Tohoku University, Sendai, Japan

[2]Frontier Research Institute for Interdisciplinary Sciences, Tohoku University, Sendai, Japan

[*] Corresponding author: Yuxian Meng

Postal address: Fracture and Reliability Research Institute, Tohoku University, 6-6-11-703, Aoba, Aramaki, Aoba-ku, Sendai 980-8579, Japan

Email ID: meng.yuxian@rs.tus.ac.jp

Abstract

Underwater cold spray (UCS) is a promising low-temperature technique for repairing protective coatings on submerged components, but the effects of processing parameters and surrounding water remain poorly understood. Here, blended Sn–Zn powder was deposited onto 304 stainless steel by low-pressure UCS, and the effects of water depth, traverse speed, gas pressure, gas temperature, and stand-off distance were investigated, supported by single-particle impact simulations. At a water depth of 25 mm, the deposition efficiency decreased from 32% in air to 2%, no Zn was detected, and the substrate temperature dropped substantially. Reducing the traverse speed to 5 mm/s yielded a continuous coating. Increasing the gas pressure from 0.4 to 0.6 MPa moderately reduced the deposition efficiency but raised the Zn area fraction from 2% to 23%. The coating delaminated at a gas temperature of 623 K, and no coating formed at a stand-off distance of 10 mm. Simulations showed that a 4 μm water film dissipated approximately 12% and 22% of the kinetic energy of Sn and Zn particles, respectively, before impact. UCS coating formation is thus governed by gas–water interaction at the jet scale and water-film energy dissipation at the particle scale, the latter preferentially suppressing Zn deposition.

Keywords

underwater cold spray; Sn–Zn coating; water film; gas–water interaction; deposition efficiency; impact simulation

Nomenclature

Abbreviations

CFD	Computational fluid dynamics
CS	Cold spray
DE	Deposition efficiency
EOS	Equation of state
GP	Gas pressure
GT	Gas temperature
SEM	Scanning electron microscope
SOD	Stand-off distance
TS	Traverse speed

UCS	Underwater cold spray
WD	Water depth

Latin symbols

A	Initial yield stress, MPa
B	Hardening constant, MPa
C	Strain rate constant
C_0	Isentropic speed of sound, m/s
E_m	Internal energy per unit volume, J/m^3
FR	Powder feeding rate, g/min
G	Shear modulus, GPa
G_0	Reference shear modulus, GPa
G'_P	Derivative of G with respect to P at the reference state
G'_T	Derivative of G with respect to T at the reference state, MPa/K
m	Thermal softening exponent
n	Work hardening exponent
n'	Hardening exponent
P	Pressure, MPa
R	Particle radius, μm
s	Material constant
t	Spray time, min
T	Temperature, K
T_m	Melting temperature, K
T_r	Reference temperature, K
v	Specific volume, m^3/kg
v_0	Initial specific volume, m^3/kg
Δm	Mass gain of the specimen after spraying, g
Y	Yield stress, MPa
Y_{max}	Maximum yield stress, MPa
Y_0	Reference yield stress, MPa
Y'_P	Derivative of Y to P at the reference state

Greek symbols

β	Work hardening constant
Γ_0	Grüneisen coefficient
$\dot{\varepsilon}$	Strain rate, 1/s
$\dot{\varepsilon}_p$	Equivalent plastic strain rate, 1/s
ε_p	Equivalent plastic strain
$\dot{\varepsilon}_0$	Reference strain rate, 1/s
η	Compression ratio, v_0/v
η'	Nominal volumetric compressive strain
δ	Water film thickness, μm
ρ	Density, kg/m^3
ρ_0	Reference density, kg/m^3

1. Introduction

Cold spray (CS) is a solid-state deposition process in which micron-sized particles, typically 1–50 μm in diameter, are accelerated to velocities of approximately 300–1200 m/s by a heated supersonic gas jet, with air, nitrogen, or helium commonly used as the process gas (Refs. 1–3). Unlike conventional thermal spray processes, CS deposits particles without melting them. Bonding is generally associated with severe plastic deformation and adiabatic shear instability at the particle–substrate or particle–particle interface (Refs. 4, 5). The relatively low processing temperature minimizes oxidation, thermal degradation, residual thermal stress, and undesirable phase transformations. Consequently, CS has attracted considerable attention for coating deposition (Ref. 6), component repair (Ref. 7), surface strengthening (Ref. 8), and additive manufacturing (Ref. 9).

Among these applications, the repair of damaged protective coatings is particularly important for extending the service life of engineering components. Such coatings may deteriorate or delaminate during service because of environmental exposure, mechanical loading, impact, or interfacial defects. Various techniques, including thermal spraying (Ref. 10), plasma nitriding (Ref. 11), and chemical-paste-based repair (Ref. 12), have been developed to restore damaged coatings. However, underwater repair remains challenging because the surrounding water affects heat transfer, material deposition, and interfacial bonding, thereby limiting the applicability of many conventional repair processes.

Several thermal processes have been investigated for underwater coating deposition. Laser cladding has been applied underwater using both wire and powder feedstocks (Refs. 13–15). The surrounding water can substantially alter heat transfer, cooling and solidification conditions, and the resulting coating characteristics. Underwater plasma spraying has also been shown to produce self-fluxing Ni-based hardfacing coatings with relatively homogeneous microstructures, low porosity, and no apparent cracks, although coating formation was highly sensitive to the nozzle stand-off distance (Ref. 16). These studies demonstrate the feasibility of underwater coating deposition using thermal processes. However, such processes involve substantial thermal input and may promote oxidation, undesirable phase transformations, residual stresses, and thermal distortion, motivating the development of lower-temperature deposition techniques.

Underwater cold spray (UCS) has recently emerged as a lower-temperature alternative for underwater coating deposition. Liu et al. (Ref. 17) demonstrated the deposition of aluminum coatings by UCS and observed greater particle deformation under water than in air. Their single-particle impact simulations indicated that deposition could occur when the particle impact velocity was sufficiently high. As a spray-based, solid-state process, UCS may offer operational advantages for localized and on-site repair compared with laser cladding. Its low thermal input also avoids bulk melting and reduces the risks of oxidation and undesirable phase transformations. Nevertheless, the effects of processing parameters on UCS coating characteristics have not been systematically investigated, and the influence of the water film on particle deposition remains insufficiently understood.

In this study, a blended Sn – Zn powder was selected as the feedstock because of its potential for protecting iron and ferrous alloys against corrosion, particularly through the sacrificial anodic action of Zn (Refs. 18, 19). A low-pressure cold spray system was employed because its compact and portable configuration is well suited to on-site repair applications (Refs. 20, 21). The effects of water depth, traverse speed, gas pressure, gas temperature, and nozzle stand-off distance on UCS coating formation were systematically examined. Surface morphology, cross-sectional microstructure, deposition efficiency, and Zn area fraction were characterized to determine how processing

conditions influence coating development. Particle-impact simulations were further conducted to elucidate the influence of a water film on particle impact and deposition at the substrate surface. The overall objective was to clarify the relationships among UCS processing conditions, water-film effects, particle deposition behavior, and the resulting coating characteristics.

2. Materials and Methods

2.1 Materials

The feedstock was prepared by blending Sn and Zn powders at a mass ratio of 1:1. As shown in Fig. 1, the Zn powder consisted predominantly of spherical particles with a nominal average diameter of 3 μm, whereas the Sn powder exhibited an irregular morphology with a nominal average diameter of 15 μm (Ref. 22). Grade 304 stainless steel was used as the substrate material.

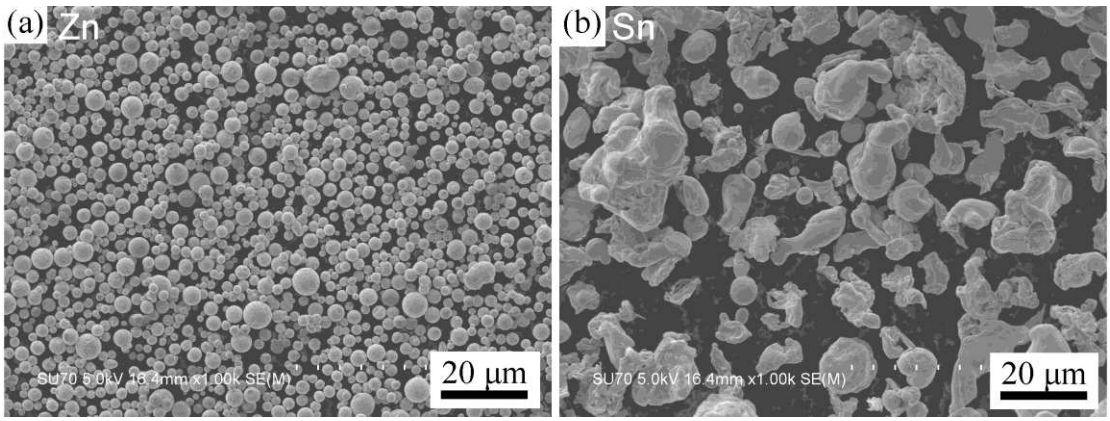


Fig. 1 Morphologies of the (a) Zn and (b) Sn powders.

2.2 Cold Spray Experiments

Figure 2 shows the experimental setup used for the cold spray tests. A rectangular tank filled with tap water was used to provide the underwater environment. A gas outlet at the top of the tank vented the process gas. The water volume was assumed to remain approximately constant during spraying because only a negligible amount of water was expelled from the tank.

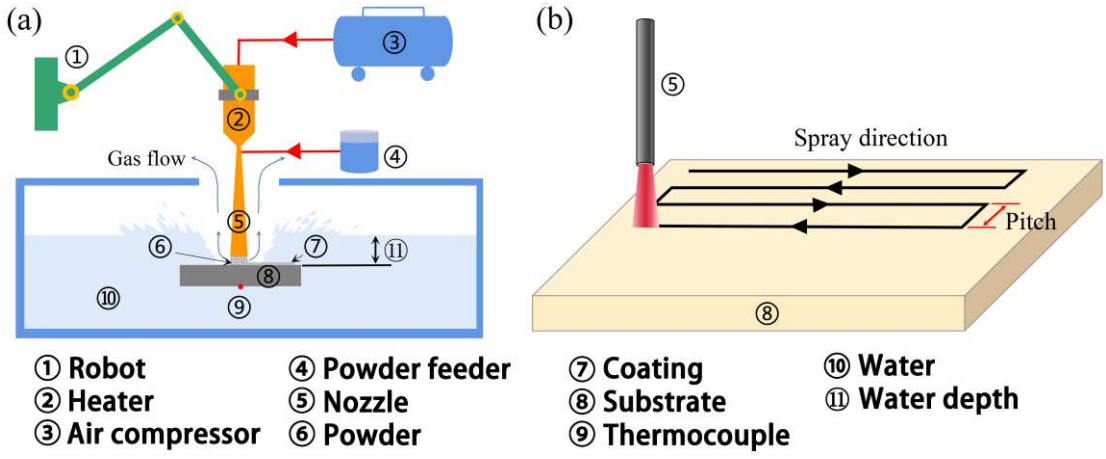


Fig. 2 (a) Schematic diagram of the experimental setup, (b) the nozzle traverse path.

A grade 304 stainless steel substrate with dimensions of 50 × 50 × 2 mm³ was clamped horizontally in a vise and immersed in water. The experiments were conducted using a commercial low-pressure cold spray system (DYMET 423, Obninsk Center for Powder Spraying, Russia). The spray gun was oriented normal to the substrate surface, and the nozzle was immersed in water during underwater spraying. During coating deposition, the nozzle traversed over the substrate according to the prescribed processing conditions.

The substrate temperature was measured using a thermocouple attached to the rear surface of the substrate. The thermocouple was aligned with the nozzle centerline, as illustrated in Fig. 2(a). For the temperature measurements, the nozzle was held stationary above the substrate. Each measurement was continued for approximately 35 s, by which time the measured temperature had reached a steady state.

The experimental conditions are summarized in Table 1. Cold spray experiments were first conducted in air and underwater at a water depth (WD) of 25 mm to evaluate the influence of the underwater environment on coating formation. Here, WD was defined as the vertical distance from the water surface to the substrate surface. An additional experiment was conducted at WD = 0 mm, in which only the backside of the substrate was in contact with water, to isolate the cooling effect of water below the substrate. The effects of traverse speed (TS), gas pressure (GP), gas temperature (GT), and stand-off distance (SOD) on the underwater cold spray process were also systematically investigated.

Table 1 Experimental conditions.

Items	**Values**
Environment	Air, water depth (WD)=0/25 mm
Traverse speed (TS)	5/10/20 mm/s
Stand-off distance (SOD)	5/10 mm
Gas pressure (GP)	0.4/0.5/0.6 MPa
Gas temperature (GT)	523/623 K
Pitch	2 mm
Pass number	1

2.3 Coating Characterization

After spraying, the specimens were dried and weighed using an analytical balance with a resolution of 0.01 mg. The deposition efficiency (*DE*) of the resulting coatings was calculated by:

$$DE = \frac{\Delta m}{FR \times t} \times 100\% \quad \text{(Eq 1)}$$

where Δm is the mass gain of the specimen, g. *FR* is the powder feeding rate (4.98 ± 0.62 g/min; mean ± SD of five measurements), and *t* is the spray time of one specimen, min.

Macroscopic images of the coatings were taken with a digital camera (Canon EOS M). The coating cross-section was mechanically polished before observation using polishing suspensions of 9 μm, 3 μm, and 0.05 μm. The microstructure of the coatings was observed by a scanning electron microscope (SEM, Hitachi FESEM SU-70). The Zn area fraction in the coating was measured by image analysis (ImageJ) of ten randomly selected cross-sectional SEM images with a magnification of ×1500.

2.4 Impact Simulation

The impact simulation was implemented in ANSYS Autodyn 2020R2 using the Eulerian method to investigate the effect of the water film thickness on the Sn/Zn particle impact deformation behavior. The Eulerian method is often used for CS particle impact simulation because it accommodates large deformation without the severe mesh distortion encountered in Lagrangian simulations (Ref. 23). Fig. 3 shows the model dimensions. A 2D axisymmetric model was adopted for the simulation. Two particle materials, Sn and Zn, were simulated impacting a Sn target, which represents particle impact onto the previously deposited Sn-rich coating. The Sn and Zn particle diameters were 15 and 3 μm, respectively. In our previous research (Ref. 22), computational fluid dynamics (CFD) simulations were carried out under the spray conditions (GP=0.4 MPa, GT=523 K, SOD=5 mm) in air for Sn and Zn particles. The details of the calculation, boundary conditions, and computational domain are given in Ref. 22. Here, only the particle temperature and velocity are listed in Table 2 for Sn and Zn.

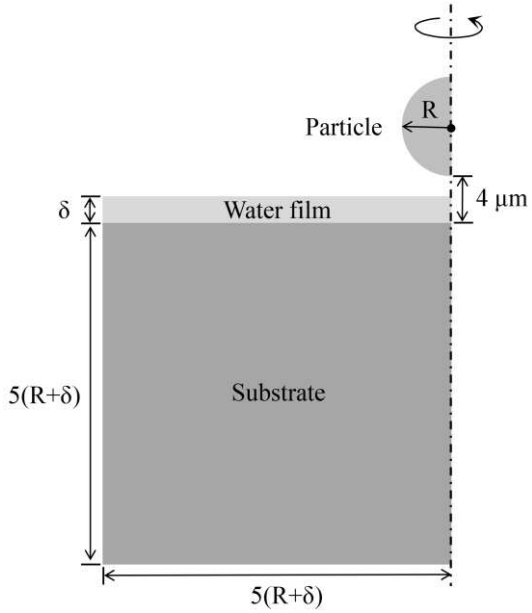


Fig. 3 Schematic of the particle impact simulation: the particle vertically impacts the substrate where a water film is located on its surface. R and δ refer to the particle radius and water film thickness, respectively.

Table 2 Material properties and average velocity and temperature of Sn (15 μm) and Zn (3 μm) particles upon impact on the substrate. The particle velocity and temperature were calculated by CFD simulations in our previous research (Ref. 22).

Materials	Density (kg/m^3)	Specific heat (J/(kg K))	Melting temperature (K)	Average particle velocity (m/s)	Average particle temperature (K)
Sn	7310	217	505	280±5	380±3
Zn	7140	380	693	293±30	468±6

Following Liu et al. (Ref. 17), the water film on the substrate surface was considered. Different film thicknesses were investigated: 0, 1, 2, and 4 μm. A fine mesh equal to R/25, where R is the

particle radius, was used for meshing the particle, water film, and impact region of the substrate. A relatively coarse mesh was used elsewhere.

The water behavior was described by the Mie-Grüneisen equation of state (EOS) in ANSYS Autodyn. This EOS is linear in internal energy and is widely used for materials subjected to high-velocity impact. The corresponding relation between pressure P and internal energy E_m is (Ref. 23):

$$P = \frac{\rho_0 C_0^2 \eta'}{(1-s\eta')^2}\left(1 - \frac{\Gamma_0 \eta'}{2}\right) + \Gamma_0 \rho_0 E_m \quad \text{(Eq 2)}$$

where ρ_0 is the reference density. C_0 is the speed of sound. s is a material constant, $\eta' = 1 - (\rho_0/\rho)$ is the nominal volumetric compressive strain. Γ_0 is the Grüneisen coefficient. E_m is the internal energy per unit volume. The corresponding material properties and parameters are shown in Table 3.

Table 3 Material properties and parameters for water (Ref. 24).

	Unit	Value
Density, ρ_0	kg/m^3	1000
Speed of sound, C_0	m/s	1483
s	—	1.75
Grüneisen coefficient, Γ_0	—	0.28

Tables 4 and 5 present the material parameters for Sn and Zn, respectively, used in the impact simulation. The elastic response of Sn and Zn was described by a linear EOS based on the bulk modulus, together with the shear modulus (Tables 4 and 5). The plastic behavior of Sn was calculated using the Steinberg-Guinan strength model (Ref. 25), while the Johnson-Cook strength model (Ref. 23) was used for Zn. The Steinberg-Guinan model defines the shear modulus (G) and yield stress (Y) as a function of strain, pressure (P), and temperature (T) for a strain rate $\dot{\varepsilon} \geq 10^5$ s^{-1} (Ref. 25), which makes it suitable for CS particle impact, where strain rates typically range from 10^5-10^8 s^{-1} (Refs. 26, 27).

$$G = G_0\left\{1 + \left(\frac{G_P'}{G_0}\right)\frac{P}{\eta^{1/3}} + \left(\frac{G_T'}{G_0}\right)(T - 300)\right\} \quad \text{(Eq 3)}$$

$$Y = Y_0\left\{1 + \left(\frac{Y_P'}{Y_0}\right)\frac{P}{\eta^{1/3}} + \left(\frac{G_T'}{G_0}\right)(T - 300)\right\}\left(1 + \beta\varepsilon_p\right)^n \quad \text{(Eq 4)}$$

subject to the limit

$$Y_0\left(1 + \beta\varepsilon_p\right)^n \leq Y_{max} \quad \text{(Eq 5)}$$

where $\eta = v_0/v$ is the compression ratio. β is the work hardening constant. n is the work hardening exponent. ε_p is the equivalent plastic strain. Y_{max} is the maximum yield stress. The subscript $_0$ refers to the reference state (T=300 K, P=0 MPa, ε_p=0). $G_P' = \frac{dG}{dP}$, $G_T' = \frac{dG}{dT}$, and $Y_P' = \frac{dY}{dP}$ are the derivatives of G and Y with respect to P or T at the reference state.

Table 4 Material properties and parameters for Sn (Refs. 28, 29).

	Unit	Value
Density	kg/m^3	7278

Specific heat	J/(kg K)	220
Bulk modulus (T=380 K)	GPa	41
Shear modulus, G_0 (T=380 K)	GPa	16.65
Yield stress, Y_0	MPa	160
Maximum yield stress, Y_{max}	MPa	220
Hardening constant, β	—	2000
Hardening exponent, n	—	0.06
Derivative $G'_P = \frac{dG}{dP}$	—	1.55
Derivative $G'_T = \frac{dG}{dT}$	MPa/K	-37.95
Derivative $Y'_P = \frac{dY}{dP}$	—	0.01386
Melting temperature	K	505

Table 5 Material properties and parameters for Zn (Refs. 30, 31).

	Unit	Value
Density	kg/m^3	7140
Specific heat	J/(kg K)	377
Bulk modulus (T=468 K)	GPa	64
Shear modulus (T=468 K)	GPa	36
Yield stress, A	MPa	82.51
Hardening constant, B	MPa	288.34
Hardening exponent, n'	—	0.1786
Strain rate constant, C	—	0.0202
Reference strain rate, $\dot{\varepsilon}_0$	s^{-1}	1
Reference temperature, T_r	K	300
Melting temperature, T_m	K	693
Thermal softening exponent, m	—	0.843

For Zn, the Johnson-Cook model was used to compute its plastic behavior. This model defines the constitutive relationship between the yield stress Y and the equivalent plastic strain ε_p, equivalent plastic strain rate $\dot{\varepsilon}_p$, and temperature T as (Ref. 23):

$$Y = \left(A + B\varepsilon_p^{n'}\right)\left(1 + C\ln\left(\frac{\dot{\varepsilon}_p}{\dot{\varepsilon}_0}\right)\right)\left(1 - \frac{T-T_r}{T_m-T_r}\right)^m \quad \text{(Eq 6)}$$

The first bracketed term in Eq. 6 represents the effect of strain hardening, where A, B, and n' are the initial yield stress at low strain, strain hardening constant, and exponent, respectively. The second parenthesis represents the effect of the strain rate, where C and $\dot{\varepsilon}_0$ are the strain rate constant and reference strain rate, respectively. The third parenthesis represents the effect of thermal softening, where T_r, T_m, and m are the reference temperature, melting temperature, and thermal softening exponent, respectively.

3. Results and Discussion

3.1 Effect of the Water Environment

Cold spray experiments were conducted in air and at water depths (WDs) of 0 and 25 mm under otherwise identical spraying conditions (GP = 0.4 MPa, GT = 523 K, SOD = 5 mm, and TS = 20 mm/s) to evaluate the influence of the water environment on coating formation. The resulting surface morphologies are shown in Fig. 4. Continuous coatings were obtained in air and at WD = 0 mm, whereas spraying at WD = 25 mm produced a discontinuous deposit consisting of numerous isolated deposition spots. These results indicate that the presence of a water layer above the substrate strongly suppresses particle deposition.

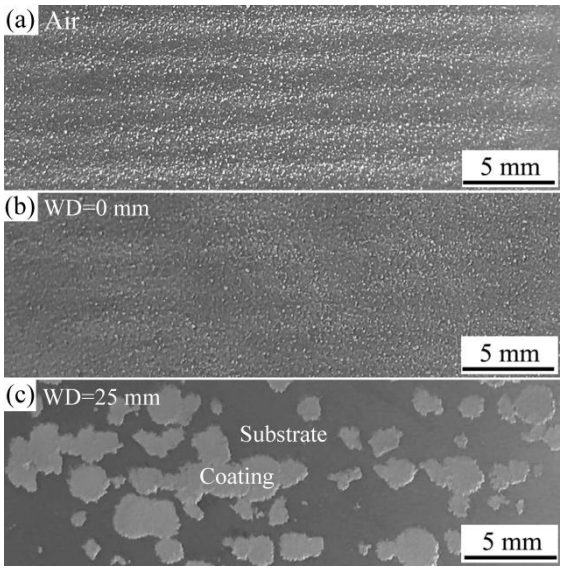


Fig. 4 Top-view photographs of coatings sprayed under GP=0.4 MPa, GT=523 K, SOD=5 mm, TS=20 mm/s in (a) air, (b) WD=0 mm, and (c) WD=25 mm. The pitch was set at 2 mm.

Two water-related effects may contribute to the discontinuous deposition observed at WD = 25 mm: resistance from the water film on the substrate or deposit surface and disturbance of the gas–particle jet. Liu et al. (Ref. 17) showed that a water film can dissipate particle kinetic energy before particle–substrate contact and thereby reduce the probability of deposition. Consistent with this mechanism, the coating deposited at WD = 25 mm exhibited numerous impact craters (Fig. 5) and a much lower deposition efficiency (~2% versus ~32% in air) than those produced in air and at WD = 0 mm, with no detectable Zn in the deposit (Figs. 6–7). Because the Zn particles were substantially smaller than the Sn particles, their deposition was expected to be more sensitive to the resistance imposed by the water film, as examined below using particle-impact simulations.

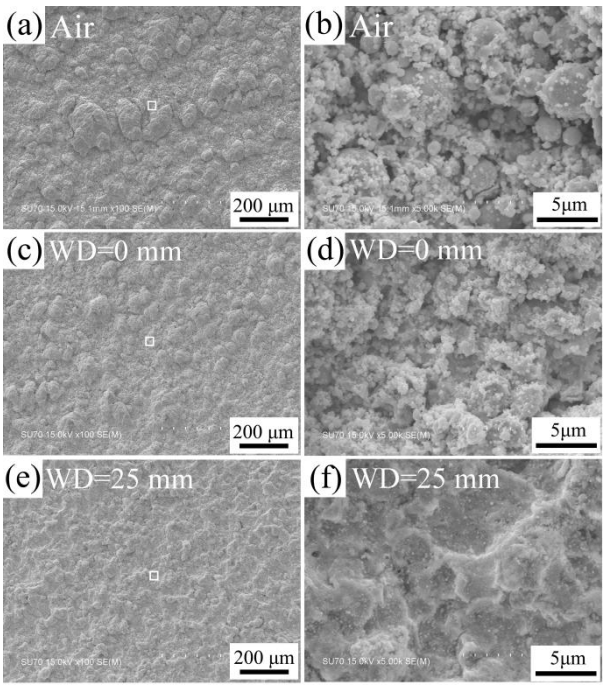


Fig. 5 Surface morphology of the coating obtained using the CS conditions (GP=0.4 MPa, GT=523 K, SOD=5 mm, TS=20 mm/s) in (a)-(b) air; (c)-(d) WD=0 mm; and (e)-(f) WD=25 mm. (b), (d) and (f) are magnified views of the boxed regions in (a), (c), and (e), respectively.

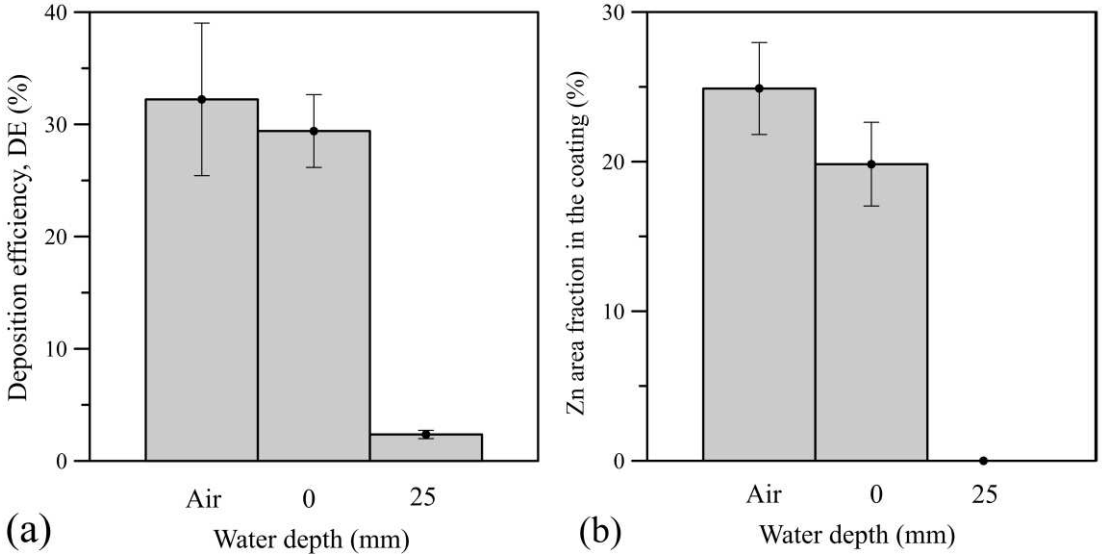


Fig. 6 Effect of the environment (air, WD=0 mm/25 mm) on the (a) deposition efficiency, (b) Zn area fraction in the coating. The corresponding CS conditions are (GP=0.4 MPa, GT=523 K, SOD=5 mm, TS=20 mm/s).

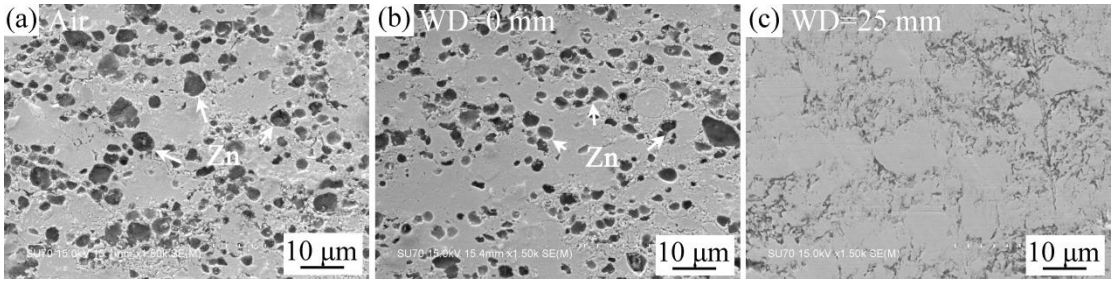


Fig. 7 Coating cross-section microstructure obtained under the CS conditions (GP=0.4 MPa, GT=523 K, SOD=5 mm, TS=20 mm/s) in (a) air, (b) WD=0 mm, and (c) WD=25 mm.

The underwater gas jet may also contribute to the reduction in deposition. Figure 8 schematically illustrates the spherical-bubble model commonly used to describe the behavior of an underwater gas jet. High-velocity gas injection into water generates an unsteady gas–liquid interface and pressure fluctuations near the nozzle outlet (Refs. 32–34). These effects can increase the hydrodynamic resistance acting on the jet and may reduce the effective gas and particle velocities. In addition, underwater gas injection can exhibit a periodic back-attack phenomenon associated with the expansion and contraction of the gas cavity (Refs. 32, 35, 36). Penetration of the gas–water mixture into the jet core may intermittently disturb particle transport and contribute to the discontinuous deposition observed in Fig. 4(c). Because the particle velocity and local jet pressure were not directly measured in the present study, this interpretation is based on the reported behavior of underwater gas jets (Refs. 32–36).

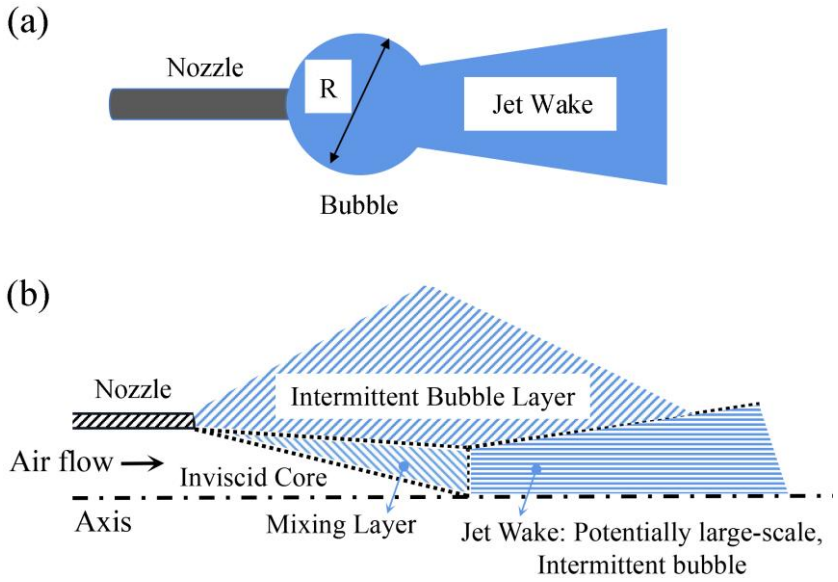


Fig. 8 (a) Schematic of the spherical bubble model (Ref. 32). The bubble diameter continuously varies during spraying, leading to a periodically occurring back-attack. (b) Schematic highlighting several regions of the flow structure in underwater jetting. The CFD simulation shows an inviscid jet core, a mixing layer where the inviscid jet and fluid diffuse, and the jet wake, which contains potentially large-scale, intermittent bubbles (Ref. 34). An intermittent layer of bubbles and droplets also forms.

Water also affected coating formation through substrate cooling. Figure 9 compares the substrate-

temperature histories under the three environmental conditions. At WD = 0 mm, contact between the backside of the substrate and water caused only a modest decrease in substrate temperature relative to spraying in air, accompanied by relatively small changes in deposition efficiency and Zn area fraction. In contrast, the substrate temperature decreased substantially at WD = 25 mm. This difference suggests that the agitated water above the substrate removed heat more rapidly than the relatively quiescent water below it.

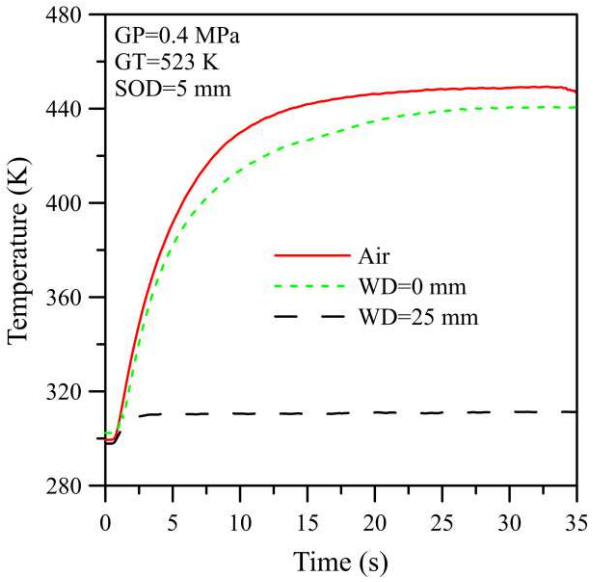


Fig. 9 Substrate backside temperature evolution directly beneath the nozzle axis in different environments. The nozzle did not move during temperature measurement, and the duration was around 35 s.

Substrate temperature is known to influence cold spray deposition. Fukumoto et al. (Ref. 37) reported an increase in copper deposition efficiency with increasing substrate temperature, while Yin et al. (Ref. 38) showed that substrate heating promotes interfacial deformation and mechanical interlocking through thermal softening. Therefore, the lower substrate temperature at WD = 25 mm may have reduced the deformability of the substrate and deposited material, thereby decreasing the probability of stable bonding. The surface morphologies in Fig. 5 are consistent with this interpretation: coatings produced in air and at WD = 0 mm contained more deposited particles, whereas the WD = 25 mm surface was dominated by impact craters.

The critical velocity for cold spray deposition is also temperature dependent. Chaban et al. (Ref. 39) reported that the critical velocity decreases as substrate temperature increases. Accordingly, the higher substrate temperatures measured in air and at WD = 0 mm would be expected to facilitate deposition relative to WD = 25 mm. This is consistent with the higher deposition efficiencies and Zn area fractions obtained under these conditions.

Overall, the water environment affected coating formation through the combined effects of substrate cooling, water-film resistance, and underwater-jet instability. These effects substantially reduced the probability of particle deposition at WD = 25 mm.

3.2 Effect of Traverse Speed

The previous results showed that a continuous UCS coating could not be obtained at TS = 20

mm/s under the selected underwater conditions. Therefore, the traverse speed was reduced to increase the local exposure time and the amount of powder delivered to the substrate.

Figure 10 shows the coating morphologies obtained at different traverse speeds. The coating coverage increased progressively as the traverse speed decreased. At TS = 20 mm/s, deposition remained highly discontinuous. Reducing the traverse speed to 10 mm/s substantially increased the coated area, although isolated uncoated regions were still present. A continuous coating was obtained at TS = 5 mm/s.

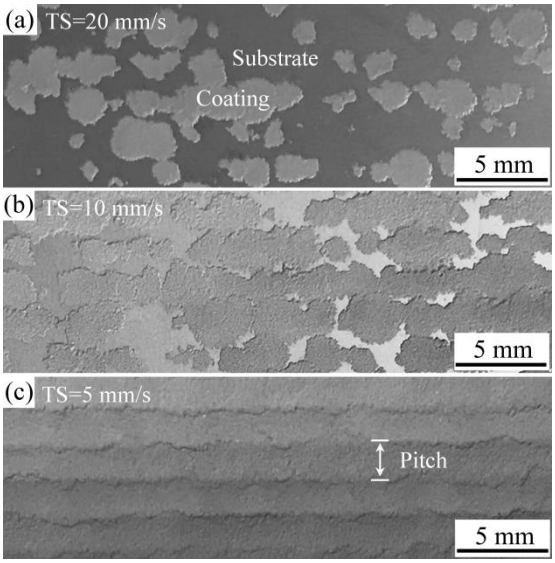


Fig. 10 Top-view photographs of coatings sprayed under GP=0.4 MPa, GT=523 K, SOD=5 mm, WD=25 mm and (a) TS=20 mm/s, (b) TS=10 mm/s, and (c) TS=5 mm/s. The pitch was set at 2 mm.

A lower traverse speed increases the residence time of the spray over a given substrate area and therefore increases the number of particles delivered per unit area. Because the underwater jet delivers particles intermittently, a higher local particle dose allows isolated deposits to overlap and merge into a continuous coating.

As shown in Fig. 11, the deposition efficiency increased from ~2.3% at TS = 20 mm/s to ~4.5% at 10 mm/s and ~9.4% at 5 mm/s. Because DE is normalized by the amount of powder fed, this increase cannot be explained by the larger particle dose alone. A plausible explanation is that, at lower traverse speeds, the initial deposits form a continuous Sn–Zn layer more quickly, so that subsequent particles increasingly impact previously deposited material rather than the bare stainless-steel substrate. Because the soft Sn–Zn deposit deforms more readily than the hard 304 stainless steel, particle–deposit bonding is expected to be easier than particle–substrate bonding. In addition, the longer local dwell time of the gas jet may help displace the water film from the impact region. These results demonstrate that traverse speed is a key parameter for achieving continuous coating formation and acceptable deposition efficiency in UCS.

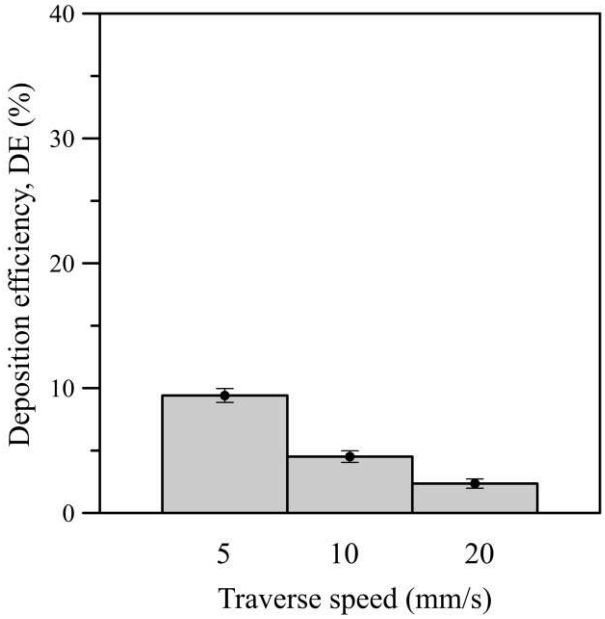


Fig. 11 Effect of the traverse speed (TS=5, 10, 20 mm/s) on the deposition efficiency. The corresponding CS conditions are (GP=0.4 MPa, GT=523 K, SOD=5 mm, WD=25 mm).

3.3 Effect of Gas Pressure

The effects of gas pressure were investigated at GP = 0.4, 0.5, and 0.6 MPa. As shown in Fig. 12, continuous coatings without obvious cracking or delamination were obtained at all three pressures, indicating that the coating integrity was maintained within the investigated pressure range.

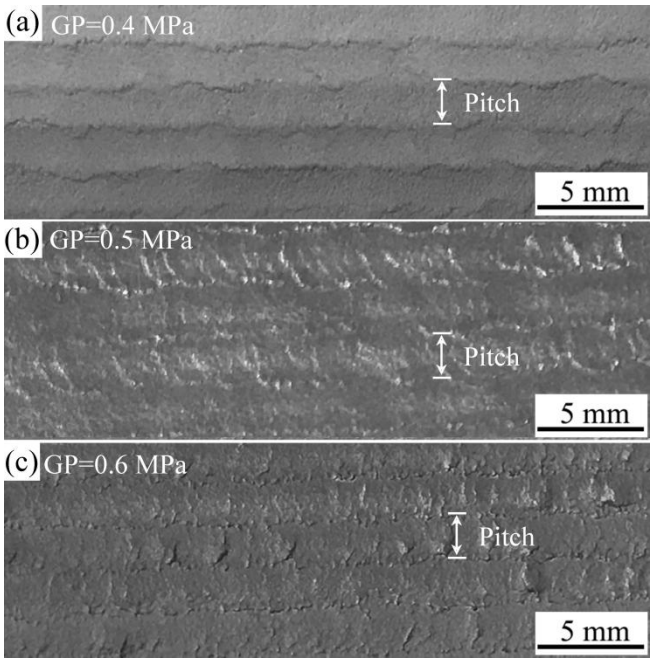


Fig. 12 Top-view photographs of coatings sprayed under GT=523 K, SOD=5 mm, TS=5 mm/s, WD=25 mm and (a) GP=0.4 MPa, (b) GP=0.5 MPa, and (c) GP=0.6 MPa. The pitch was set at 2 mm.

Figure 13(a) shows that the deposition efficiency decreased from ~9.4% at 0.4 MPa to ~8.2% at

0.5 MPa and ~6.2% at 0.6 MPa. A similar trend was observed in our previous low-pressure cold spray study using the same powder system (Ref. 22). At relatively high particle velocities, rebound and erosion of previously deposited material may become increasingly important. This decrease in deposition efficiency observed here may therefore reflect an increased erosion or rebound contribution at higher gas pressure. A similar trend was reported by Che et al. and Liberati et al. (Refs. 40–42), who attributed the decrease in Sn deposition efficiency with increasing gas pressure to more pronounced erosion.

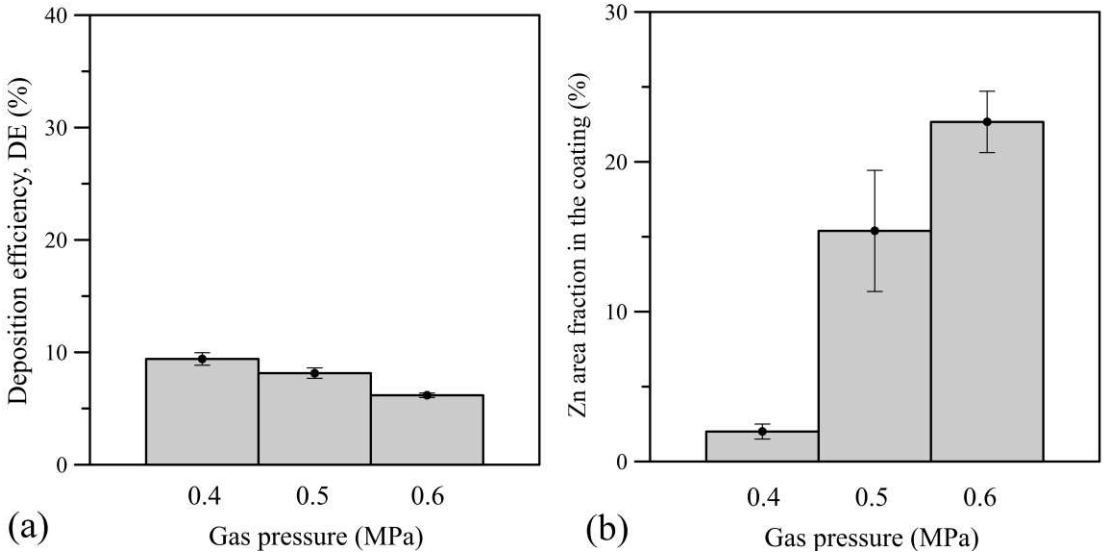


Fig. 13 Effect of the gas pressure (GP=0.4, 0.5, 0.6 MPa) on the (a) deposition efficiency, (b) Zn area fraction in the coating. The corresponding CS conditions are (GT=523 K, SOD=5 mm, TS=5 mm/s, WD=25 mm).

In contrast, the Zn area fraction increased markedly as the gas pressure increased from 0.4 to 0.6 MPa, as shown in Figs. 13(b) and 14. Increasing gas pressure generally increases particle velocity and can therefore improve the ability of the smaller Zn particles to overcome the resistance associated with the water film. The substrate-backside temperature increased by only ~10 K (Fig. 15), suggesting that substrate thermal softening had little effect on the increase in Zn area fraction.

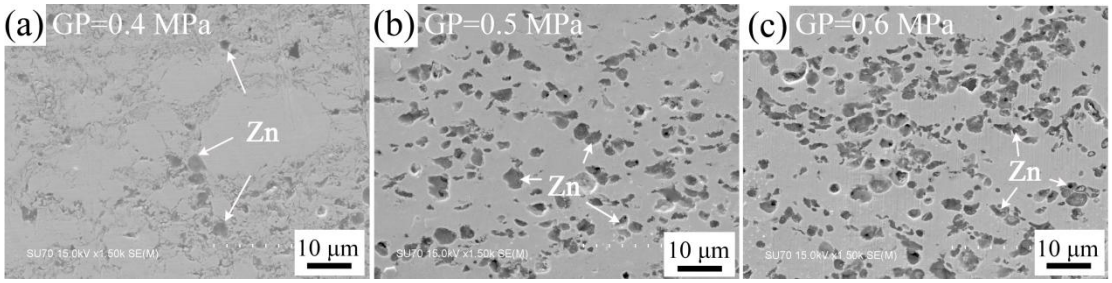


Fig. 14 Coating cross-section microstructure obtained for different gas pressures under the CS conditions (GT=523 K, SOD=5 mm, TS=5 mm/s, WD=25 mm), and (a) GP=0.4 MPa, (b) GP=0.5 MPa, and (c) GP=0.6 MPa.

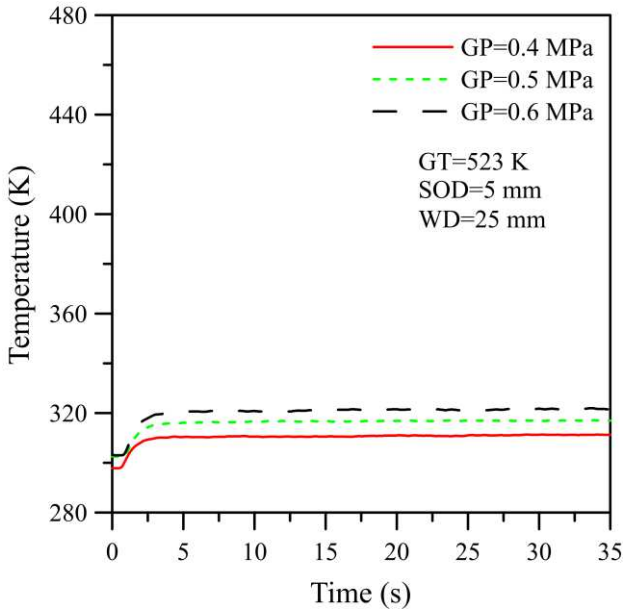


Fig. 15 Substrate backside temperature evolution directly beneath the nozzle axis for different gas pressures. The nozzle did not move during the temperature measurement, and the duration was around 35 s.

Thus, increasing the gas pressure produced two opposite trends: it reduced the overall deposition efficiency by about one-third, possibly because of enhanced rebound or erosion, while substantially increasing the incorporation of Zn into the coating. Gas pressure therefore provides an effective means of controlling the composition of Sn–Zn coatings deposited by UCS.

3.4 Effect of Gas Temperature

The influence of gas temperature was investigated at 523 and 623 K under otherwise identical conditions (GP = 0.4 MPa, SOD = 5 mm, TS = 5 mm/s, and WD = 25 mm). As shown in Fig. 16, a continuous coating was obtained at 523 K, whereas no adherent coating remained on the substrate after spraying at 623 K. Coating fragments were recovered from the water tank after the 623 K experiment, indicating that deposition occurred initially but was followed by delamination.

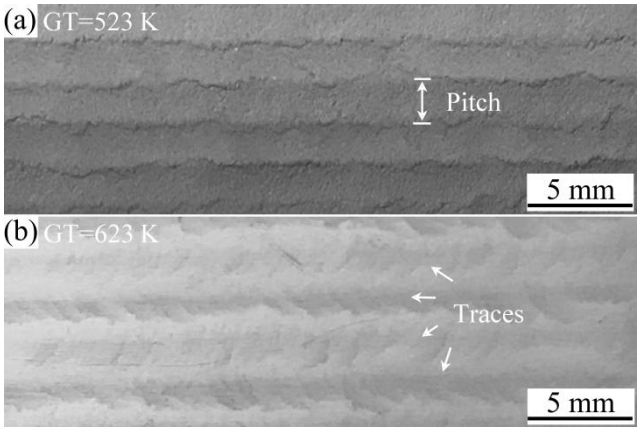


Fig. 16 Top-view photographs of coatings sprayed under GP=0.4 MPa, SOD=5 mm, TS=5 mm/s, WD=25 mm, and (a) GT=523 K and (b) GT=623 K. At 623 K, only traces remained after the coating

detached.

Increasing the gas temperature generally increases both particle and substrate temperatures and can reduce the critical velocity for cold spray deposition (Refs. 43, 44). For UCS, however, the substrate-backside temperatures at gas temperatures of 523 and 623 K differed only slightly (Fig. 17), possibly because agitated water enhanced heat removal. This suggests that the higher particle temperature, rather than a substantial increase in substrate temperature, may have played a dominant role in the observed delamination.

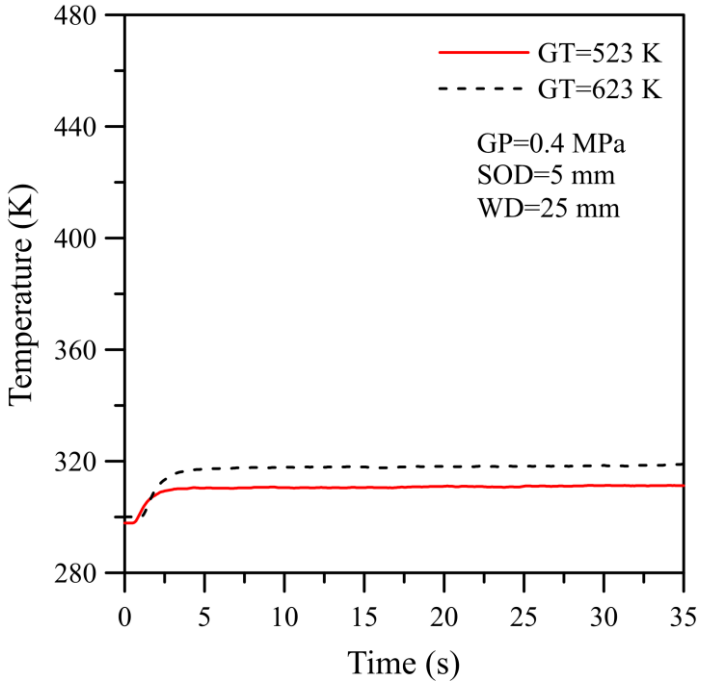


Fig. 17 Substrate backside temperature evolution directly beneath the nozzle axis for different gas temperatures. The nozzle did not move during temperature measurement, and the duration was around 35 s.

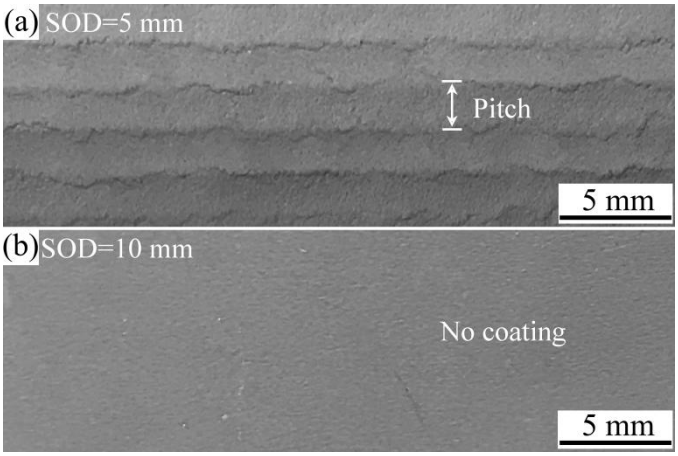


Fig. 18 Top-view photographs of coatings sprayed under GP=0.4 MPa, GT=523 K, TS=5 mm/s, WD=25 mm, and (a) SOD=5 mm and (b) SOD=10 mm.

In the present Sn–Zn/304 stainless steel system, thermal-expansion mismatch is expected to contribute to interfacial stress development because the coefficients of thermal expansion of Sn and Zn are higher than that of 304 stainless steel (Ref. 45). Suhonen et al. (Ref. 46) showed that thermal and quenching effects can generate tensile residual stresses, whereas particle peening tends to generate compressive stresses. Because Sn and Zn are considerably softer than the stainless-steel substrate, the peening contribution at the coating–substrate interface may be relatively limited. Taken together, these observations suggest that the delamination at 623 K is most likely caused by increased tensile stresses arising from the larger temperature drop of the hotter particles upon quenching by the substrate and surrounding water, combined with the thermal-expansion mismatch between the Sn–Zn coating and the stainless-steel substrate.

3.5 Effect of Stand-Off Distance

The effect of stand-off distance was investigated at SOD = 5 and 10 mm under otherwise identical conditions (GP = 0.4 MPa, GT = 523 K, TS = 5 mm/s, and WD = 25 mm). A continuous coating was obtained at SOD = 5 mm, whereas no coating was observed at SOD = 10 mm (Fig. 18). No coating fragments were found in the water tank after the 10 mm test, suggesting that particle deposition was strongly suppressed rather than followed by coating detachment.

The reduced deposition at the larger stand-off distance is likely associated with stronger interaction between the gas–particle jet and the surrounding water. As the stand-off distance increases, particles remain in the gas–water mixing region for a longer time, increasing the likelihood of momentum loss and trajectory deviation before impact on the substrate. The periodic penetration of the gas–water mixture into the jet core may further disturb particle transport at locations farther from the nozzle outlet.

Fronzeo et al. (Ref. 34) reported that the inviscid-core length of an underwater gas jet can be approximately twice the nozzle-exit diameter under comparable pressure-ratio conditions. Based on the present nozzle outlet diameter of 4.8 mm, the corresponding characteristic length is ~9.6 mm. This rough estimate suggests that a stand-off distance of 10 mm places the substrate near or beyond the region where the jet begins to experience substantial interaction with the surrounding water. This provides a plausible explanation for the strong deterioration in coating deposition observed at SOD = 10 mm.

3.6 Deposition Mechanism

Figure 19 compares single-pass tracks deposited in air and under water. In air, a continuous track was formed at TS = 5 mm/s (Fig. 19(a)). Under water, isolated deposits were obtained at TS = 20 mm/s (Fig. 19(b)), whereas reducing the traverse speed to 5 mm/s increased the local particle dose and allowed the individual deposits to overlap into a continuous track (Fig. 19(c)).

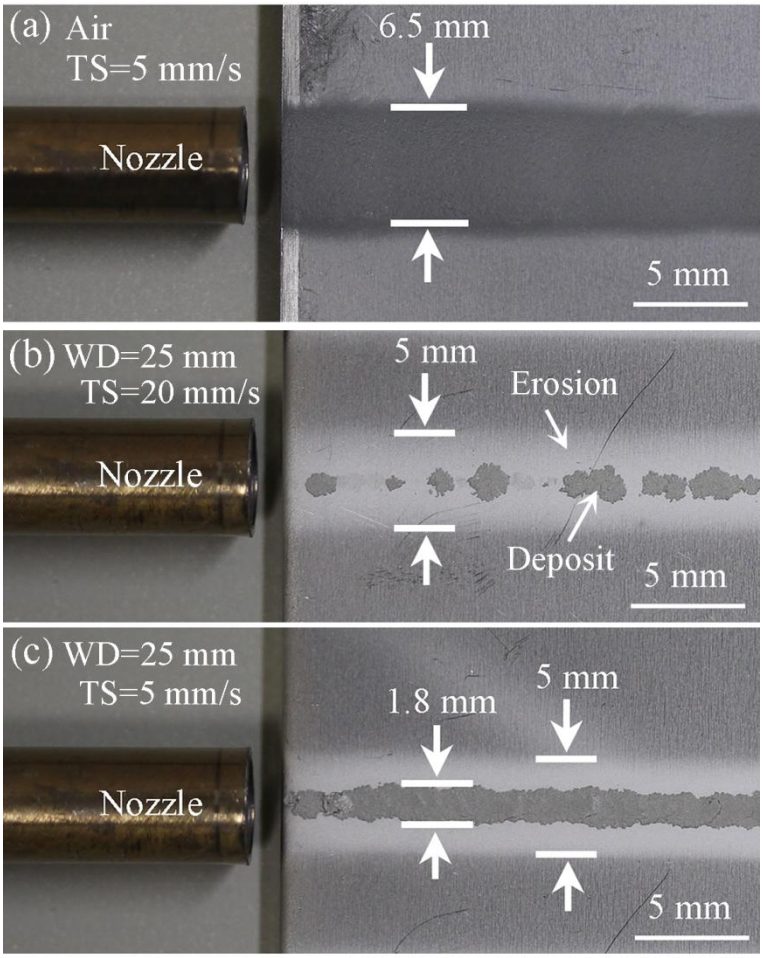


Fig. 19 Single-pass tracks deposited under GP = 0.4 MPa, GT = 523 K, and SOD = 5 mm: (a) in air, TS = 5 mm/s; (b) WD = 25 mm, TS = 20 mm/s; (c) WD = 25 mm, TS = 5 mm/s.

At the same traverse speed of 5 mm/s, the underwater track was considerably narrower than the track deposited in air (~1.8 mm versus ~6.5 mm; Figs. 19(a) and 19(c)), and it was flanked by an eroded band approximately 5 mm wide. This indicates that particles reached the periphery of the jet but deposited only near the nozzle centerline. As shown schematically in Fig. 8(b), the water fraction in the jet increases with radial distance from the jet core. Particles traveling through this two-phase region are therefore more likely to experience momentum loss and trajectory deviation, which reduces their probability of reaching the substrate with sufficient velocity for deposition.

In addition to the jet-scale effects, the water film on the substrate plays an important role in individual particle deposition. Liu et al. (Ref. 17) showed numerically that an interfacial water film can reduce particle impact energy and may remain trapped between the particle and substrate when sufficiently thick. To further examine this effect for the present Sn–Zn system, single-particle impact simulations were performed for Sn and Zn particles with different water-film thicknesses.

Figures 20(a) and 20(b) show the kinetic-energy histories of Sn and Zn particles impacting the substrate with and without a water film. For both particle species, the kinetic energy at contact decreased progressively as the water-film thickness increased. The energy loss began when the particle interacted with the film, before direct contact with the substrate. As shown in Fig. 20(c), compression of the water generated a high-pressure region in front of the particle, resulting in rapid

particle deceleration. The fractional kinetic-energy loss was greater for Zn particles than for Sn particles (Fig. 20(d)), which can be attributed to their smaller size and lower inertia, making them more susceptible to deceleration by the water film.

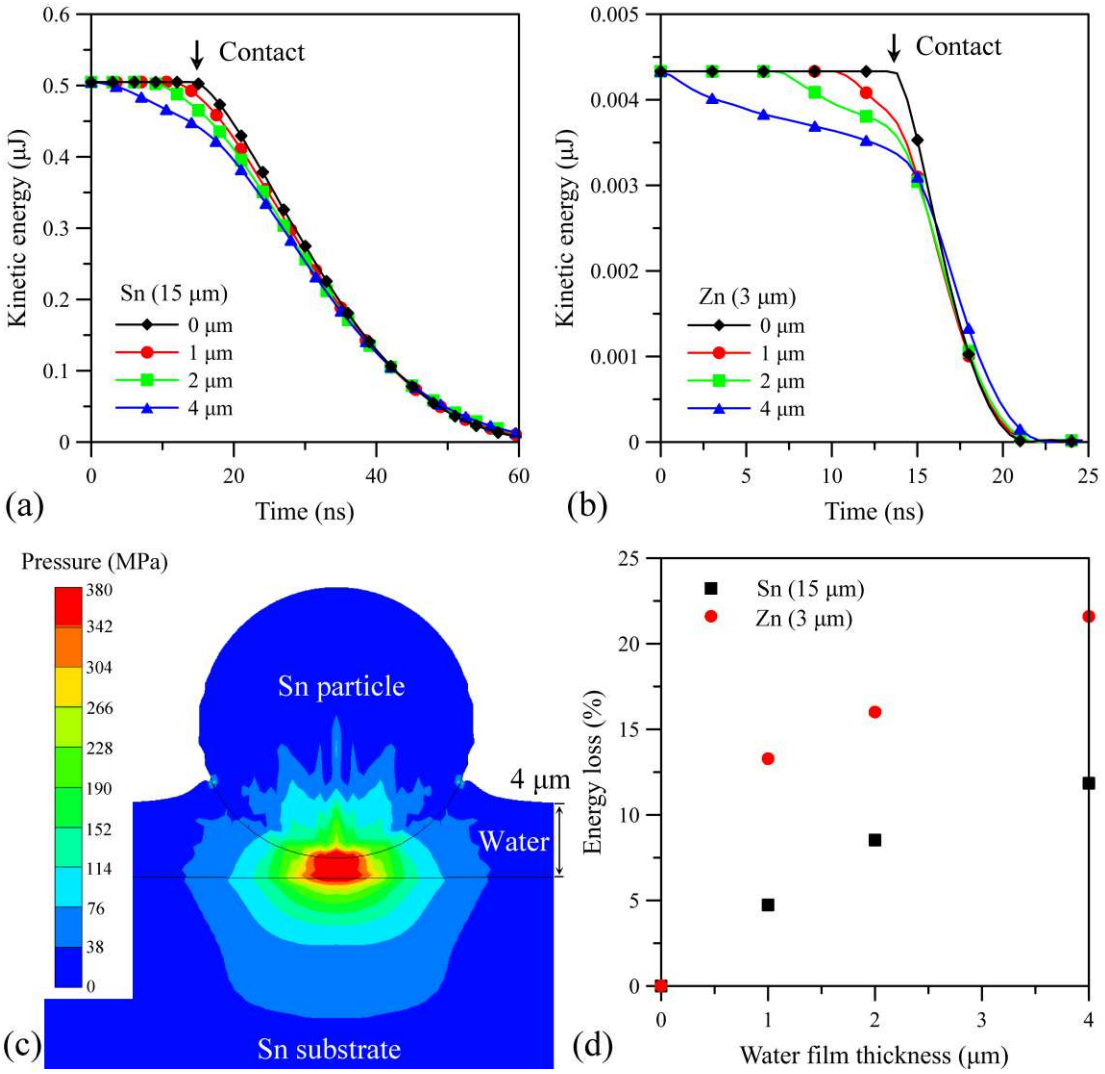


Fig. 20 Kinetic energy evolution of (a) Sn and (b) Zn particles for different water film thicknesses. (c) Pressure contour upon the impact of the particle: a Sn particle impacted the Sn substrate with a 4 μm thick water film. The initial velocity and temperature of the particle were set at 280 m/s and 380 K, respectively (see Table 2). (d) Energy loss of Sn/Zn particles before contact with the substrate. Arrows in (a) and (b) mark the initial contact between the particle and substrate.

The combined experimental and numerical results therefore suggest that UCS coating formation is governed by two coupled mechanisms. At the jet scale, gas–water interaction causes intermittent and spatially non-uniform particle delivery. At the particle scale, the water film dissipates particle kinetic energy before substrate contact. Because the smaller Zn particles experience a larger fractional energy loss, their deposition is more strongly suppressed, resulting in a lower Zn area fraction at WD = 25 mm. These mechanisms explain the strong sensitivity of UCS coating formation to traverse speed, gas pressure, and stand-off distance observed in the present study.

4. Conclusion

Sn–Zn coatings were deposited on 304 stainless steel by low-pressure underwater cold spray. The effects of the water environment and the main processing parameters were investigated through experiments and single-particle impact simulations. The main conclusions are as follows:

1. The water environment strongly suppressed deposition. At WD = 25 mm and TS = 20 mm/s, the deposit was discontinuous, the deposition efficiency decreased from about 32% (in air) to about 2%, and no Zn was detected. When only the substrate backside was in contact with water (WD = 0 mm), coating formation changed little. This indicates that the water above the substrate, rather than backside cooling alone, was responsible for the deterioration.
2. Water above the substrate lowered the substrate temperature substantially (about 311 K, compared with about 448 K in air). This likely reduced the deformability of the substrate and the deposited material and raised the critical velocity, decreasing the probability of bonding.
3. Reducing the traverse speed to 5 mm/s increased the local particle dose. It allowed the isolated deposition regions to overlap into a continuous coating and raised the deposition efficiency to about 9%.
4. Increasing the gas pressure from 0.4 to 0.6 MPa lowered the deposition efficiency from about 9.4% to 6.2%, possibly through enhanced rebound or erosion. At the same time, it increased the Zn area fraction in the coating from about 2% to about 23%. Gas pressure therefore offers an effective way to control coating composition in UCS.
5. At GT = 623 K, the coating deposited but subsequently delaminated. This is most likely caused by increased tensile stresses arising from the higher particle temperature and the thermal-expansion mismatch between Sn–Zn and the stainless steel substrate. At SOD = 10 mm, no coating formed, consistent with stronger gas–water interaction beyond the inviscid jet core.
6. Impact simulations showed that an interfacial water film dissipates particle kinetic energy before contact with the substrate. The fractional loss was larger for the 3 μm Zn particles than for the 15 μm Sn particles, which explains the preferential loss of Zn under underwater conditions.

Within the investigated ranges, continuous UCS coatings were obtained at TS = 5 mm/s, GT = 523 K, SOD = 5 mm, and GP = 0.4–0.6 MPa. Future work will focus on improving deposition efficiency by limiting gas–water mixing in the free-jet region, for example through nozzle designs that shield the jet or allow a shorter stand-off distance. The porosity, adhesion strength, and residual stress of UCS Sn–Zn coatings will also be evaluated.

Acknowledgments

The authors thank Tohoku University and Fukushima Daiichi D&D Engineering Company, TEPCO Holdings, Inc., for funding the joint research project "Research and Development for Decommissioning Fukushima Daiichi Nuclear Power Plants."
The authors gratefully acknowledge the Institute of Fluid Science, Tohoku University, for supporting this research under its Collaborative Research Project (Grant No. J21Ly17).

Conflict of Interest

The authors have no relevant financial or non-financial interests to disclose.

Author Contributions

Yuxian Meng: Conceptualization, Data curation, Formal analysis, Investigation, Methodology, Validation, Visualization, Writing – original draft. **Hiroki Saito**: Supervision, Writing–review and editing. **Chrystelle A. Bernard**: Funding acquisition, Project administration, Supervision, Writing–review and editing. **Yuji Ichikawa**: Resources, Supervision. **Kazuhiro Ogawa**: Funding acquisition, Project administration, Resources, Supervision.

References

[1] R.N. Raoelison, Y. Xie, T. Sapanathan, et al., Cold Gas Dynamic Spray Technology: a Comprehensive Review of Processing Conditions for Various Technological Developments Till to Date, *Addit. Manuf.*, 2018, **19**, p 134–159. https://doi.org/10.1016/j.addma.2017.07.001

[2] Y. Ichikawa, K. Shinoda, Current Status and Challenges for Unified Understanding of Bonding Mechanism in Solid Particle Deposition Process, *Mater. Trans.*, 2021, **62**(6), p 691–702. https://doi.org/10.2320/matertrans.T-M2021813

[3] H. Assadi, H. Kreye, F. Gärtner, and T. Klassen, Cold Spraying - A Materials Perspective, *Acta Mater.*, 2016, **116**, p 382–407. https://doi.org/10.1016/j.actamat.2016.06.034

[4] W.Y. Li, C.C. Cao, G.Q. Wang, et al., 'Cold Spray +' As a New Hybrid Additive Manufacturing Technology: a Literature Review, *Sci. Technol. Weld. Join.*, 2019, **24**, p 420–445. https://doi.org/10.1080/13621718.2019.1603851

[5] H. Assadi, F. Gärtner, T. Stoltenhoff, H. Kreye, Bonding Mechanism in Cold Gas Spraying, *Acta Mater.,* 2003, **51**(15), p 4379–4394. https://doi.org/10.1016/S1359-6454(03)00274-X

[6] Y. Ichikawa, K. Ogawa, I. Nonaka, High-Temperature Oxidation Behavior of Cold-Sprayed MCrAlY Coatings, *Zair./J. Soc. Mater. Sci. Jpn.*, 2011, **60**(2), p 159–166. https://doi.org/10.2472/jsms.60.159

[7] K. Ogawa, D. Seo, Repair of Turbine Blades Using Cold Spray Technique, *Advances in Gas Turbine Technology*, 2011, p 500–526. https://doi.org/10.5772/23623

[8] N. Yamaguchi, T. Shiozaki, Y. Tamai, et al., Effect of Cold Spray Deposition on Fatigue Strength of Arc-Welded Ultra-High Strength Steel Sheet, *Int. J. Fatigue*, 2022, **161**, p 106876. https://doi.org/10.1016/j.ijfatigue.2022.106876

[9] X.T. Luo, M.L. Yao, N.S. Ma, M. Takahashi, and C.J. Li, Deposition Behavior, Microstructure and Mechanical Properties of an In-Situ Micro-Forging Assisted Cold Spray Enabled Additively Manufactured Inconel 718 Alloy, *Mater. Des.,* 2018, **155**(5), p 384–395. https://doi.org/10.1016/j.matdes.2018.06.024

[10] F. Rousseau, C. Guyon, D. Morvan, et al., Low Power Plasma Spray Assisted Thermal Barrier Coating Repair Without the Plugging of Cooling Holes, *Surf. Coat. Technol.,* 2021, **421**, p 127050. https://doi.org/10.1016/j.surfcoat.2021.127050

[11] S.H. Sarraf, M. Soltanieh, H. Aghajani, Repairing the Cracks Network of Hard Chromium Electroplated Layers Using Plasma Nitriding Technique, *Vacuum*, 2016, **127**, p 1–9. https://doi.org/10.1016/j.vacuum.2016.02.001

[12] X. Yang, J. Zhang, Z. Lu, et al., Removal and Repair Techniques for Thermal Barrier Coatings: A Review, *Trans. IMF*, 2020, **98**(3), p 121–128. https://doi.org/10.1080/00202967.2020.1750204

[13] Q. Cheng, N. Guo, Y.L. Fu, et al., Investigation on In-Situ Laser Cladding 5356 Aluminum Alloy Coating on 5052 Aluminum Alloy Substrate in Water Environment, *J. Mater. Res. Technol.*, 2021, **15**, p 4343–4352. https://doi.org/10.1016/j.jmrt.2021.10.073

[14] Y.L. Fu, N. Guo, C. Zhou, G.H. Wang, J.C. Feng, Investigation on In-Situ Laser Cladding Coating of the 304 Stainless Steel in Water Environment, *J. Mater. Process. Technol.*, 2021, **289**, p 116949. https://doi.org/10.1016/j.jmatprotec.2020.116949

[15] X.R. Feng, X.F. Cui, G. Jin, et al., Underwater Laser Cladding in Full Wet Surroundings for Fabrication of Nickel Aluminum Bronze Coatings, *Surf. Coat. Technol.,* 2018, **333**, p 104–114. https://doi.org/10.1016/j.surfcoat.2017.10.056

[16] E. Lugscheider, B. Hauser, B. Bugsel, Underwater Plasma Spraying of Hardsurfacing Alloys, *Surf. Coat. Technol.,* 1987, **30**, p 73–81. https://doi.org/10.1016/0257-8972(87)90009-0

[17] Y. Liu, C.X. Li, X.F. Huang, et al., Effect of Water Environment on Particle Deposition of Underwater Cold Spray, *Appl. Surf. Sci.,* 2020, **506**, p 144542. https://doi.org/10.1016/j.apsusc.2019.144542

[18] M.Y. Rekha, A. Kamboj, C. Srivastava, Electrochemical Behaviour of SnZn-Graphene Oxide Composite Coatings, *Thin Solid Films,* 2017*,* **636**, p 593–601. https://doi.org/10.1016/j.tsf.2017.07.004

[19] O.S. Fatoba, A.P.I. Popoola, T. Fedotova, Characterization and Corrosion Behavior of Zn-Sn Binary Alloy Coatings in 0.5 M H_2SO_4 Solution, *J. Electrochem. Sci. Technol.*, 2015, **6**(2), p 65–74. https://doi.org/10.33961/jecst.2015.6.2.65

[20] K. Ogawa, K. Ito, K. Ichimura, et al., Characterization of Low-Pressure Cold-Sprayed Aluminum Coatings, *J. Therm. Spray Technol*., 2008, **17**, p 728–735. https://doi.org/10.1007/s11666-008-9254-5

[21] R.G. Maev, V. Leshchynsky, Low-Pressure Cold Spray (LPCS). In: Cavaliere, P. (ed.) Cold-Spray Coatings. Springer, Cham. 2018. p 95–142. https://doi.org/10.1007/978-3-319-67183-3_4

[22] Y. Meng, H. Saito, C. Bernard, Y. Ichikawa, K. Ogawa, Parametric Study to Repair Leaks in Water Pipe Using the Low-Pressure Cold Spray Technique, *J. Therm. Spray Technol*., 2022, **31**, p 2560–2576. https://doi.org/10.1007/s11666-022-01469-y

[23] A. Fardan, C.C. Berndt, R. Ahmed, Numerical Modelling of Particle Impact and Residual Stresses in Cold Sprayed Coatings: A Review, *Surf. Coat. Technol*., 2021, **409**, p 126835. https://doi.org/10.1016/j.surfcoat.2021.126835

[24] D.A. Matuska, HULL Users' Manual, Technical Report AFATL-TR-84-59, Air Force Armament Laboratory, Eglin Air Force Base, FL, 1984 (DTIC Accession No. ADA145000).

[25] D.J. Steinberg, S.G. Cochran, M.W. Guinan, A Constitutive Model for Metals Applicable at High-Strain Rate, *J. Appl. Phys*., 1980, **51**, p 1498–1504. https://doi.org/10.1063/1.327799

[26] V. Lemiale, P.C. King, M. Rudman, et al., Temperature and Strain Rate Effects in Cold Spray Investigated by Smoothed Particle Hydrodynamics, *Surf. Coat. Technol*., 2014, **254**, p 121–130. DOI: 10.1016/j.surfcoat.2014.05.071

[27] R.C. Dykhuizen, M.F. Smith, D.L. Gilmore, et al., Impact of High Velocity Cold Spray Particles, *J. Therm. Spray Technol*., 1999, **8**, p 559–564. https://doi.org/10.1361/105996399770350250

[28] M.H. Nadal, P. Le Poac, Continuous Model for the Shear Modulus As a Function of Pressure and Temperature Up to the Melting Point: Analysis and Ultrasonic Validation, *J. Appl. Phys.*,

2003, **93**, p 2472–2480. https://doi.org/10.1063/1.1539913

[29] D.J. Steinberg, Equation of State and Strength Properties of Selected Materials, Lawrence Livermore National Laboratory, 1996.

[30] Z. Wang, S. Cai, K. Jin, X. Wang, W. Chen, In-Flight Aggregation and Deposition Behaviour of Particles in Low Pressure Cold Spray, *Surf. Coat. Technol*., 2021, **409**, p 126875. DOI: 10.1016/j.surfcoat.2021.126875

[31] H.M. Ledbetter, Elastic Properties of Zinc: A Compilation and a Review, *J. Phys. Chem. Ref. Data*, 1977, **6**(4), p 1181–1203. https://doi.org/10.1063/1.555564

[32] N. Huang, Z.H. Chen, Z.L. Wang, Main Characteristics of Underwater Supersonic Gas Jet Flows, *Math. Probl. Eng.*, 2022, **2022**, p 1–16. https://doi.org/10.1155/2022/1191938

[33] X. Zhang, S. Li, D. Yu, B. Yang, N. Wang, The Evolution of Interfaces for Underwater Supersonic Gas Jets, Water, 2020, **12**(2), p 488. https://doi.org/10.3390/w12020488

[34] M. Fronzeo, M. Kinzel, An Investigation of Gas Jets Submerged in Water, *46th AIAA Fluid Dynamics Conference*, 2016. https://doi.org/10.2514/6.2016-4253

[35] T. Aoki, The Mechanism of the Back-Attack Phenomenon on a Bottom Blowing Tuyere Investigated in Model Experiments, *Tetsu-To-Hagane*, 1990, **76**(11), p 1996–2003. DOI:10.2355/TETSUTOHAGANE1955.76.11_1996

[36] Y.W. Zhang, X.H. Wang, and J.X. Yang, Study on Working Thrust for Underwater Engine Using the Spherical Bubble Model, *J. Hydrodyn.*, 2005, **20**(5), p 636–640.

[37] M. Fukumoto, H. Wada, K. Tanabe, et al., Effect of Substrate Temperature on Deposition Behavior of Copper Particles on Substrate Surfaces in the Cold Spray Process, *J. Therm. Spray Technol.*, 2007, **16**, p 643–650. https://doi.org/10.1007/s11666-007-9121-9

[38] S. Yin, X. Suo, Y. Xie, et al., Effect of Substrate Temperature on Interfacial Bonding for Cold Spray of Ni onto Cu, *J. Mater. Sci.*, 2015, **50**, p 7448–7457. https://doi.org/10.1007/s10853-015-9304-6

[39] I. Chaban, Y. Sun, D. Veysset, K.A. Nelson, C.A. Schuh, The Effect of Substrate Temperature on the Critical Velocity in Micro-Particle Impact Bonding, *Appl. Phys. Lett.*, 2021, **119**, 011903. https://doi.org/10.1063/5.0055274

[40] H. Che, X. Chu, P. Vo, S. Yue, Cold Spray of Mixed Metal Powders on Carbon Fibre Reinforced Polymers, *Surf. Coat. Technol*., 2017, **329**, p 232–243. DOI: 10.1016/j.surfcoat.2017.09.052

[41] H. Che, P. Vo, S. Yue, Metallization of Carbon Fibre Reinforced Polymers by Cold Spray, *Surf. Coat. Technol.*, 2017, **313**, p 236–247. DOI: 10.1016/j.surfcoat.2017.01.083

[42] A. Liberati, H. Che, S. Yue, P. Vo, Cold Spraying of Mixed Sn-Al Powders onto Carbon Fibre Reinforced Polymers, *International Thermal Spray Conference*, 2018, USA. https://doi.org/10.31399/asm.cp.itsc2018p0166

[43] X. Meng, J. Zhang, Y. Liang, W. Hai, J. Zhao, Effect of Gas Temperature on the Particle Deposition Characteristics and Coating Microstructure by Cold Spray, *Mater. Sci. Forum*, 2011, **675-677**, p 1295–1298. https://doi.org/10.4028/www.scientific.net/MSF.675-677.1295

[44] S. Yin, X. Suo, H. Liao, Z. Guo, X. Wang, Significant Influence of Carrier Gas Temperature During the Cold Spray Process, *Surf. Eng.*, 2014, **30**(6), p 443–450. https://doi.org/10.1179/1743294414Y.0000000276

[45] MatWeb material property data, available online at http://www.matweb.com.

[46] T. Suhonen, T. Varis, S. Dosta, M. Torrell, J.M. Guilemany, Residual Stress Development in Cold Sprayed Al, Cu and Ti Coatings, *Acta Mater.*, 2013, **61**, p 6329–6337. DOI:

10.1016/j.actamat.2013.06.033